Supplement of Atmos. Chem. Phys., 26, 9149–9180, 2026
https://doi.org/10.5194/acp-26-9149-2026-supplement

Atmospheric Chemistry and Physics
Open Access
EGU

Supplement of

Microphysical evolution and column loading drive nonlinear regional contrast in black carbon top-of-atmosphere forcing

Pravash Tiwari et al.

Correspondence to: Jason Blake Cohen (jasonbc@alum.mit.edu)

Section S1

Theoretical Concept of Santa Barbara DISORT Atmospheric Radiative Transfer Model (SBDART)

In this study, the Santa Barbara DISORT Atmospheric Radiative Transfer (SBDART) model (Ricchiazzi et al., 1998) (available at https://github.com/paulricchiazzi/SBDART) is utilized to calculate atmospheric irradiance both including and excluding aerosol influences. Given that most solar radiation is concentrated within the 0.25 to 4.0 μm wavelength range (Paulescu et al., 2013), the analysis is confined to this spectral interval. To perform these irradiance computations, SBDART requires inputs such as columnar aerosol optical depth (AOD), Single scattering albedo (SSA), and Angstrom exponent (ASY) as, per waveband optical properties. In our case we have derived BCAOD and corresponding SSA and ASY at different wavebands using a set of observational data and their uncertainties as explained in the main text. Additionally, the column water vapor, surface spectral albedo, and surface ozone data obtained from MODIS and TROPOMI satellites respectively are used to compute their respective local impacts on the radiative stream. Monthly averages of model atmosphere were prepared using temperature, pressure, and ozone vertical profiles sourced from ERA-5 reanalysis datasets (https://cds.climate.copernicus.eu/cdsapp#!/dataset/reanalysis-era5-pressure-levels?tab=form), dynamically updating the model atmosphere for each month.

The aerosol DRF is dertermined by evaluating the difference in net radiative fluxes, where the net flux (ΔF) is defined as the difference between the downward irradiance (F↓) and upward irradiance ($F^{\uparrow}$):

$$\Delta F = F_{\downarrow} - F^{\uparrow} \qquad \text{Eq. 1}$$

The net flux is calculated separately at the top of the atmosphere (TOA) and the Earth's surface(SFC). To isolate the effect of aerosols, the net flux with aerosols present (F_{aero}) is compared against the net flux without aerosols ($F_{non\text{-}aero}$). The forcing at TOA and SFC are computed by subtracting the non aerosol net flux from the aerosol net flux:

$$\Delta F_{TOA} = \Delta F_{aero,TOA} - \Delta F_{non\text{-}aero,TOA} \qquad \text{Eq. 2}$$

In this study, SBDART used its default near-surface-dominant aerosol vertical distribution, with aerosol loading concentrated within the lower atmosphere/boundary layer and decreasing with altitude. SBDART is a widely used model to analyze the aerosol DRF (Fu et al., 2017; Patel et al., 2017).

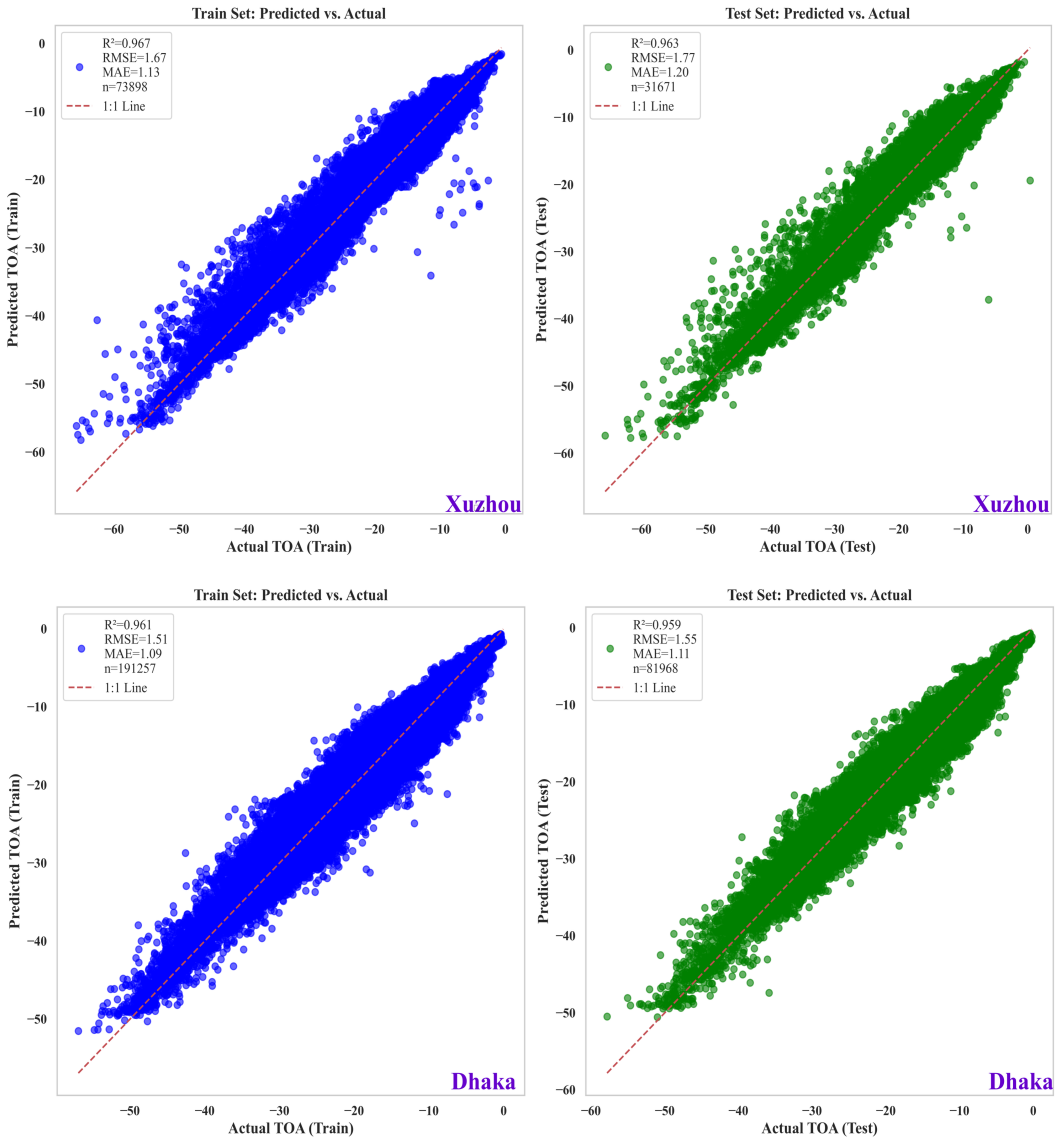

.

Figure S1: Comparison of predicted TOA values from the ML model against actual TOA values for both training and test datasets. The top row represents results for Xuzhou, while the bottom row represents Dhaka. The left panels show predictions on the training set, while the right panels show predictions on the test set. Each scatter plot includes key performance metrics: the coefficient of determination (R^2), Root Mean Square Error (RMSE), and Mean Absolute Error (MAE). The red dashed line represents the 1:1 reference line, indicating perfect agreement between predicted and actual TOA values. Model hyperparameters were set as follows: n_estimators=100, max_depth=10, min_samples_split=5, min_samples_leaf=3, max_features='sqrt' for Random Forest regressors.

Table S1: Train and Test Performance from 5-Fold Cross-Validation of the developed ML TOA Models in Xuzhou and Dhaka

Folds	Xuzhou (Train)			Dhaka (Train)		
	R^2	RMSE	MAE	R^2	RMSE	MAE
1	0.96	1.7	1.2	0.96	1.5	1.1
2	0.96	1.8	1.2	0.96	1.5	1.1
3	0.96	1.7	1.2	0.96	1.6	1.1
4	0.96	1.8	1.2	0.96	1.6	1.1
5	0.96	1.8	1.2	0.96	1.5	1.1
	Xuzhou (Test)			Dhaka (Test)		
1	0.96	1.8	1.2	0.96	1.6	1.1
2	0.96	1.8	1.2	0.96	1.6	1.1
3	0.96	1.9	1.2	0.96	1.6	1.1
4	0.96	1.7	1.2	0.96	1.5	1.1
5	0.96	1.8	1.2	0.96	1.6	1.1

Section S2

AERONET-based consistency assessment of COSMO-RTM BC TOA forcing efficiency

To evaluate whether the COSMO-RTM BC TOA forcing fields used as the machine-learning target are physically consistent with independent aerosol radiative constraints, COSMO-RTM BC TOA forcing efficiency was compared with AERONET Version 3 Level 2.0 total-aerosol forcing efficiency over Dhaka. Because AERONET provides total-aerosol radiative forcing rather than BC-isolated forcing, this analysis is not intended as a strict one-to-one validation of BC TOA DRF. Instead, it evaluates whether the COSMO-RTM BC TOA forcing efficiency shows physically consistent regime-dependent, and proportional behavior relative to AERONET total-aerosol TOA forcing efficiency under absorbing aerosol conditions.

For Dhaka, AERONET Version 3 Level 2.0 inversion retrievals of TOA DRF were matched with COSMO-RTM BC TOA DRF estimates by retaining model pixels within a 20 km radius of the AERONET station. Model grid values were aggregated to daily means to match the temporal resolution of the AERONET inversion product. AERONET AAOD at 550 nm was derived from measured absorption AAOD (440-870) and AAE, and the FE was calculated as:

$$FE_{AERONET} = \frac{\text{TOA DRF}_{AERONET}}{AAOD_{550}}$$

representing total aerosol forcing efficiency from AERONET. For the COSMO-RTM side, BC FE was calculated as:

$$FE_{BC} = \frac{\text{TOA DRF}_{BC}}{BCAAOD_{550}}$$

using COSMO-SBDART-derived BC TOA forcing and the corresponding BC absorption optical depth.

The study used AAOD rather than AOD because the purpose of this comparison is to evaluate absorbing-aerosol radiative response. For BC-specific forcing, absorption optical depth is the relevant optical driver, whereas normalization by total AOD would mix BC absorption with scattering aerosol and other non-BC absorbing components.

Regime-dependent strengthening of the COSMO-RTM and AERONET TOA FE relationship

The study examined whether the COSMO-RTM BC TOA FE and AERONET TOA FE relationship changes systematically with aerosol absorption regime (Figure S2a). Across all matched retrievals, the ordinary regression slope between $FE_{modelBC}$ and $FE_{AERONET}$ was 0.31, with a significant correlation ($R = 0.6$; $p < 0.001$). When the analysis was restricted to the more absorbing, spectrally BC-like subset, defined by cases where SSA_{440} was below the 30th percentile and $0.8 < AAE_{440\text{-}870} < 1.4$ (Liu et al., 2018; Luo et al., 2023), the slope increased to 0.63 while the relationship remained significant ($R = 0.55$; $p < 0.001$). This increase indicates that the proportional scaling between COSMO-RTM BC FE and AERONET total-aerosol FE becomes closer under more BC-like absorption conditions.

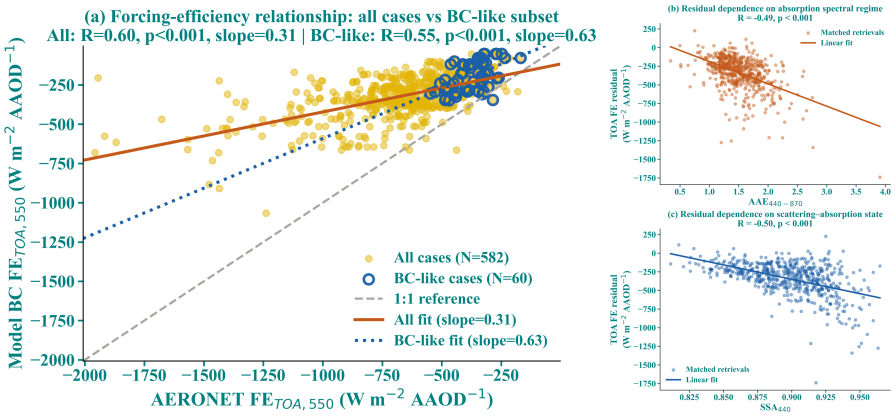

Figure S2: Regime-dependent consistency between COSMO-RTM BC TOA FE and AERONET total-aerosol TOA FE. (a) Scatterplot of COSMO-RTM BC-only TOA FE against AERONET total-aerosol TOA FE for all matched retrievals and for the spectrally BC-like subset. b) Residual dependence on AAE440-870. (c) Residual dependence on SSA440.

The residual analysis (Figure S2(b and c) further supports this regime dependence. The forcing-efficiency residual, is not randomly distributed with respect to aerosol optical state. Instead, it shows significant dependence on both $AAE_{440\text{-}870}$ and SSA_{440}. Residuals decrease systematically with increasing AAE ($R = -0.49$; $p < 0.001$), indicating that the separation between AERONET total-aerosol FE and model BC-only FE changes as the absorption spectrum becomes less BC-like (Figure S2b). A similar but slightly stronger dependence is observed with SSA_{440} ($R = -0.50$; $p < 0.001$), showing that the residual structure is also controlled by the column scattering-absorption balance (Figure S2c).

The regime-dependent analysis shows that the COSMO-RTM BC TOA FE and AERONET TOA FE relationship strenghtens under low SSA and spectrally BC like conditions and the residuals are systematically structured by AAE and SSA. These results suggest that the COSMO-RTM BC and AERONET differences are systematically organized by aerosol optical regime rather than being structureless residual scatter.

Relative-scaling diagnostic

While the regime-dependent analysis establishes that the COSMO-RTM BC TOA and AERONET TOA FE relationship strengthens under BC-like optical conditions (more absorbing conditions), it does not by itself determine whether the magnitude of COSMO-RTM BC-only FE is reasonable relative to AERONET total-aerosol FE. To address this, a relative-scaling diagnostic was used to define the expected BC-to-total aerosol benchmark.

The theoretically expected TOA FE scaling was derived from the the ratio of two separately computed fractions, independent of the fitted FE regression. The BC absorption fraction quantifies BC's contribution to total column absorption:

$$R_{abs} = \frac{\text{BC AAOD}_{550}}{\text{AAOD}_{550}^{\text{AERONET}}}$$

The BC forcing fraction quantifies the magnitude of BC TOA forcing from COSMO-RTM relative to the AERONET total-aerosol TOA forcing:

$$R_{DRF} = \frac{\left|\text{DRF}_{\text{TOA,BC}}\right|}{\left|\text{DRF}_{\text{TOA,AERONET}}\right|}$$

If the COSMO-RTM BC microphysics and radiative-transfer calculation are physically consistent with the independent AERONET total-aerosol forcing constraint, then the observed scaling between FE_{BC} and $FE_{AERONET}$ should be consistent with:

$$\text{Expected TOA FE scaling} = \frac{R_{DRF}}{R_{abs}}$$

This expectation arises because the model BC FE represents radiative effect per unit BC absorption, while AERONET total FE represents radiative effect per unit total aerosol absorption. Their ratio therefore scales with the relative contribution of BC to both absorption and TOA forcing. Importantly, this expected scaling is not fitted from the FE regression itself; rather, it provides a physically constrained benchmark for evaluating whether the BC-only FE magnitude is reasonable relative to the AERONET total-aerosol FE. It is therefore not a direct validation of isolated BC forcing, but a relative-scaling consistency test designed for the case where the observational product represents total aerosol forcing and the model isolates the BC component. Since this benchmark is a proportional ratio, it was compared with the origin-constrained COSMO-RTM TOA FE - AERONET total aerosol TOA FE slope, $FE_{BC} = mFE_{AERONET}$, rather than with the ordinary OLS slope that includes an intercept. The ordinary OLS slope was used above only to diagnose regime-dependent strengthening of the relationship.

Table S2. Relative-scaling diagnostic between COSMO-RTM BC TOA FE and AERONET total-aerosol TOA FE.

Regime	R_{abs} [95% CI]	R_{DRF} [95% CI]	Expected TOA FE scaling [95% CI]	Observed origin-constrained slope [95% CI]	Median $FE_{BC}/FE_{AERONET}$
All cases	066[0.62-0.69]	0.32[0.29-0.35]	0.48[0.44-0.53]	0.46[0.43-0.48]	0.48
BC-like subset (SSA_{440} < 30th percentile and AAE 0.8-1.4)	0.51[0.45-0.57]	0.25[0.17-0.32]	0.50[0.33-0.62]	0.53[0.46-0.61]	0.55

Table S2 shows that the observed proportional COSMO-RTM BC TOA FE - AERONET total aerosol TOA FE scaling is consistent with the expected BC-to-total aerosol benchmark. For all matched cases, the observed origin-constrained slope was 0.46 [0.43-0.48], closely overlapping the expected scaling of 0.48 [0.44-0.53]. For the BC-like subset, the observed slope increased to 0.53 [0.46-0.61], while the expected scaling was 0.50 [0.33-0.62]. The median $FE_{BC}/FE_{AERONET}$ ratio also increased from 0.48 to 0.55 under more absorbing BC-like conditions. Thus, the magnitude of COSMO-RTM BC TOA FE while is not expected to match AERONET total-aerosol TOA FE one-to-one, but it falls within the physically interpretable BC-to-total aerosol scaling range. The decrease from 0.66 to 0.51 should not be interpreted as a weakening of the FE consistency result, because R_{abs} and R_{DRF} are both recomputed for a different optically filtered subset. The relevant diagnostic is not whether R_{abs} increases or decreases, but whether the ratio R_{DRF}/R_{abs} agrees with the observed origin-constrained FE slope. This agreement is maintained for both all cases and the more absorbing BC-like subset.

Overall, this analysis supports the physical coherence of the observation-constrained COSMO-RTM BC forcing target. Although it does not constitute direct validation of isolated BC DRF, the COSMO-RTM BC TOA FE shows regime-dependent and proportional consistency with independent AERONET total-aerosol radiative forcing constraints.

Table S3: Categorizing the Predictors based on their percentiles for conditional analysis

Percentile Conditions	$BCAOD_{550}$	BC Size	Mixing-state
<25th	Clean	small	Heavily coated
>=25th &<50th	fairly polluted	medium	Moderately coated
>=50th &<75th	moderately polluted	Big	Minimally coated
>=75th	polluted	Very Big	Barely coated

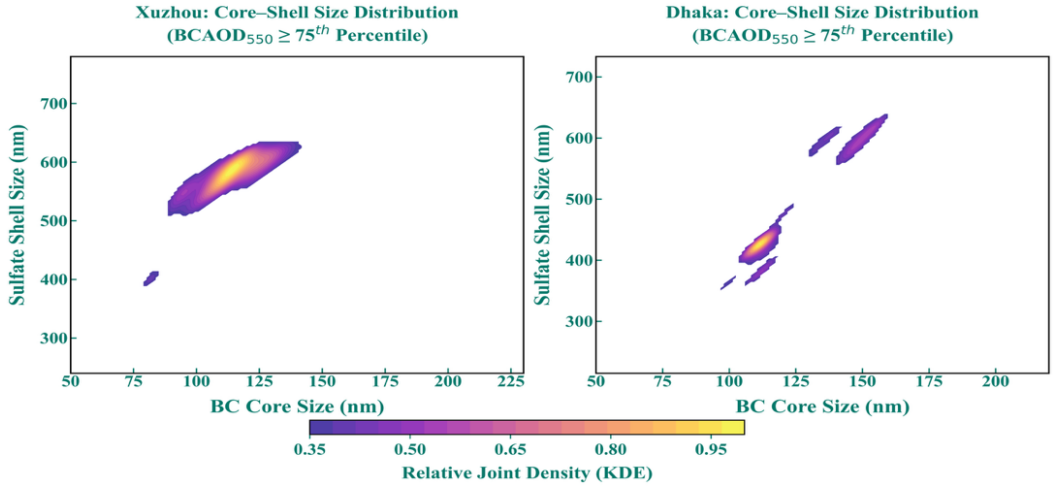

Figure S3: Dominant BC core-sulfate shell size distributions under polluted conditions ($BCAOD_{550}$ >75th percentile in Xuzhou and Dhaka. Color shading shows the relative joint KDE density normalized by the regional maximum, indicating the most frequent core–shell microphysical states during high-loading conditions.

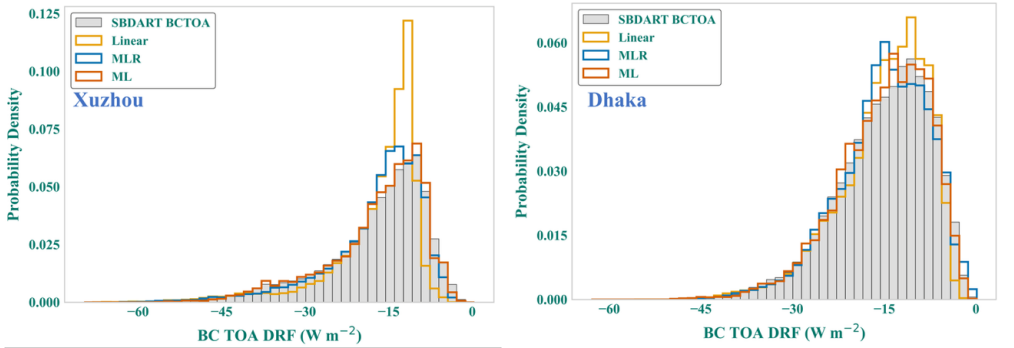

Xuzhou				
Percentile	SBDART	Linear	MLR	ML
1st	-45.4	-49.0	-47.9	-43.9
99th	-4.1	-7.2	-5.1	-4.5

Dhaka				
Percentile	SBDART	Linear	MLR	ML
1st	-37.1	-37.6	-36.5	-36.5
99th	-2.8	-4.4	-2.2	-3.1

Figure S4: Probability density functions (PDFs) of BC TOA values from SBDART and the three surrogate models (Linear, MLR, and ML) for Xuzhou (left) and Dhaka (right). Tabulated percentile

values at the 1st and 99th percentiles are provided below each panel to compare the distributional extremes.

Section S3.

Model performance comparison across different Pollution conditions.

The performance of the model was also analyzed under different pollution conditions, and has been illustrated using the Taylor Diagram (Figure S5) over Xuzhou and Dhaka. All the models demonstrate variable efficacy across pollution conditions in Xuzhou and Dhaka, with ML consistently outperforming linear and MLR approaches.

In Xuzhou, ML achieves superior correlations (0.85 to 0.96) (Figure S5), lower RMSE (1.1 to 2.3 Wm^{-2}), and enhanced variance capture especially in moderate to high pollution condition, compared to MLR and linear models. Its near-zero mean bias (MBE: −0.07 to 0.05 Wm^{-2}) across different pollution conditions and tighter 95% confidence demonstrates minimal systematic error and high precision. Under clean conditions, ML achieves a lower RMSE (1.1 Wm^{-2}), reducing errors by 48% and 59% compared to MLR and linear model. Similarly, over Dhaka, ML further excels, with bias corrected RMSE (0.9 Wm^{-2}) approximately 36% lower than MLR (1.4 Wm^{-2}) and 40% lower than linear (1.5 Wm^{-2}), underscoring ML's reliability in clean scenarios over both regions. This improvement is noteworthy because AOD and AAOD retrievals/inversions from multiple platforms, typically exhibit higher accuracy in moderate and polluted conditions, while clean conditions pose challenges due to weaker aerosol signals (Dubovik et al., 2000, 2006; Dubovik and King, 2000). The challenges in retrieving AOD and AAOD directly affect the quantification of direct radiative forcing (DRF), particularly for black carbon (BC). Our model benefits from a more size- and mixing state-flexible aerosol representation that captures aerosol physical and optical properties both more precisely and in a more physically accurate manner. This in turn results in improved radiative transfer model (RTM) simulations of BC DRF, which the ML model then reproduces with high fidelity. Under fairly and moderately polluted conditions of Xuzhou, the ML model outperforms competing methods, achieving a bias-corrected RMSE approximately 18% lower than MLR and 44% lower than the linear model. The ML model's mean bias error (MBE) is near zero; 0.01 Wm^{-2} for fairly polluted and 0.02 Wm^{-2} for moderately polluted conditions-indicating minimal bias. This contrasts with MLR, which shows a slight underprediction reflected by negative MBE (-0.2 Wm^{-2}) in fairly polluted conditions and a positive bias (0.5 Wm^{-2}) in moderately polluted conditions. Similarly, the linear model exhibits larger biases of -0.5 Wm^{-2} and 0.9 Wm^{-2} respectively for these pollution levels. The ML model's low bias paired with lower error metrics highlights its improved accuracy and reliability across these conditions.

Similar performance was observed in Dhaka, where under fairly polluted conditions, ML model achieves a bias-corrected RMSE reduction of approximately 22% compared to MLR decreasing from 1.8 to 1.4 Wm^{-2}, and even more pronounced reduction of 33% compared to linear model. Similarly, under moderate pollution condition, ML reduces bias corrected RMSE by 23% over MLR (1.7 vs. 2.2 Wm^{-2}) and by approximately 37% compared to linear model. MLR exhibits slightly enhanced prediction of the spread in Dhaka compared

to linear, however it fails to align its predictions with the SBDART trend or relationships in the observations. This indicates, while MLR might predict larger deviations from the mean at the right time (matching the variability), these deviations may be occurring in the wrong direction or phase relative to observations, and likely are driven by different underlying physics than the cleaner cases observed in Xuzhou, possibly necessitating improvements to the underlying physical model to account for this non-linearity.

Under polluted conditions in Xuzhou, ML's bias corrected RMSE is 36% and 55% lower than MLR and linear models respectively. While over Dhaka, the variance captured by ML (SBDART: 5.9 vs. ML: 5.5) also high correlation (0.94) and bias corrected RMSE reduced by more than 30%. Overall, ML offered superior reproduction ability of the underlying physical model in all conditions, with the performance gap widening as pollution magnitude strengthens.

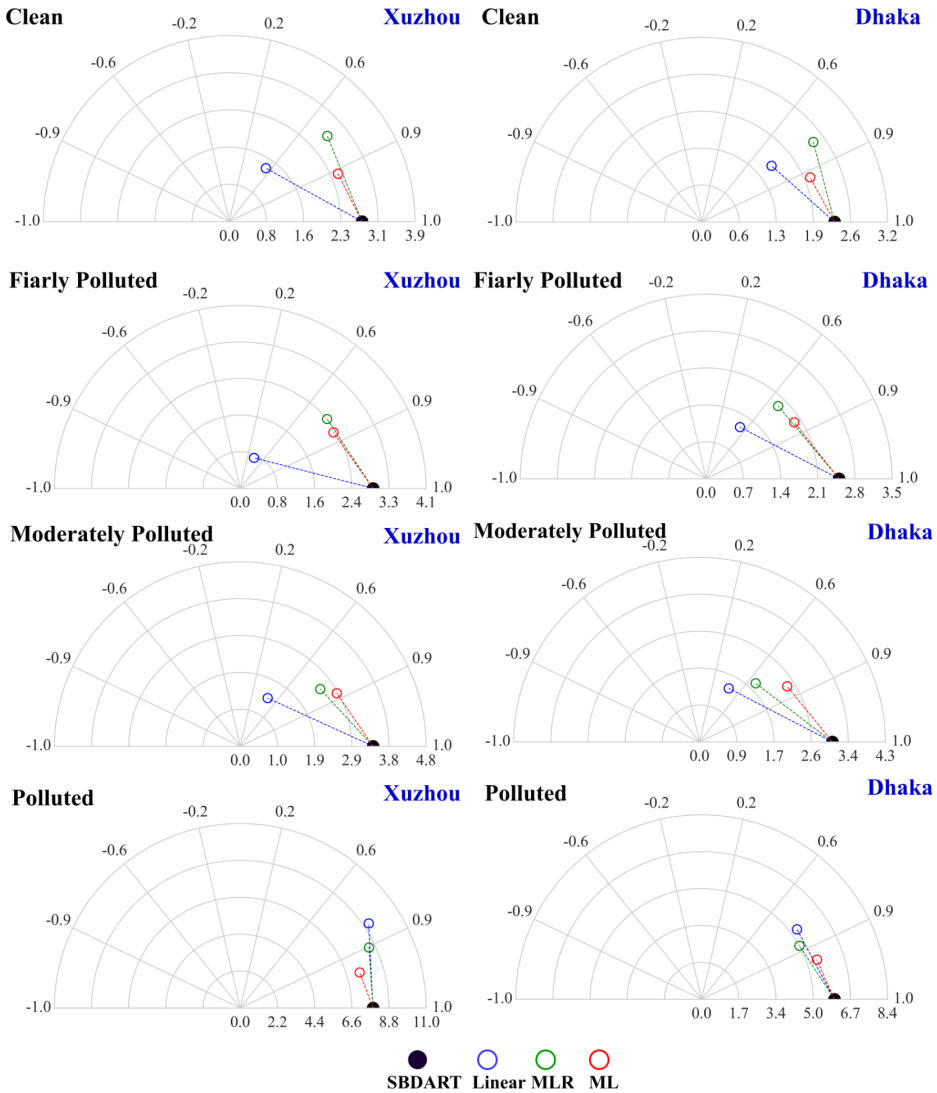

Figure S5: Taylor diagram comparing the performance of Linear, MLR, and ML models in predicting TOA radiative forcing for Xuzhou (left) and Dhaka (right) under different pollution conditions (Clean,

Fairly Polluted, Moderately Polluted, and Polluted). The diagrams illustrate the standard deviation (radial) and correlation coefficient (angular) of each model relative to SBDART (black dot). The proximity of model points to the reference (SBDART) indicates prediction accuracy, with colors representing different models.

Section S4

SHAP Analysis across different TOA regimes.

SHAP analysis performed across different BC TOA ranges (Figure S6) further elucidates how predictor importance evolves as predicted aerosol radiative effects transition from cooling to warming. In both regions, $BCAOD_{550}$ dominates the ML predicted radiative forcing, transitioning from scatter-driven cooling at high values (Xuzhou: 0.4-2.2; Dhaka: 0.41-1.9) under low TOA to absorption-driven warming at lower values (Xuzhou: 0.01-0.45; Dhaka: 0.01-0.43) under high BC TOA. Notably, overlapping BCAOD550 ranges (0.4-0.45) exhibit both positive and negative SHAP contributions (warming and cooling tendencies), consistent with competing absorption and scattering influences in the underlying RTM-derived training data, and suggesting that the model learns sensitivity to small changes in aerosol microphysics that shift the predicted overall effect. This shift is accompanied by a systematic narrowing of the range of aerosol properties associated with cooling as predicted BC TOA forcing intensifies. In Xuzhou, the upper bound of $BCAOD_{550}$ associated with cooling decreases from 2.2 (Low BC TOA) to 2.0 (High BC TOA), while in Dhaka, it narrows from 1.9 to 0.8. Concurrently, the lower bound of $BCAOD_{550}$ associated with warming shifts towards smaller values, indicating although total attenuation decreases, the plausible transition from scattering-to absorption-dominated regimes may drive the BC TOA towards more warming. These patterns emphasize that BC TOA transition is governed by coupled evolution of aerosol loading and microphysical changes.

A key regional contrast emerges in the role of mixing state, whose relative importance increases with TOA forcing, particularly from mid-high to high BC TOA conditions in Xuzhou. This growth exceeds that of N_c, despite N_c retaining a higher overall SHAP magnitude. In Dhaka, mixing-state SHAP effects peak under intermediate BC TOA conditions and weaken at high and low BC TOA, indicative of a different coupling between coating evolution and column loading. BC size plays a marginal role in both regions but gains modest importance in Dhaka's High BC TOA (75.6% positive SHAP for >220 nm cores), consistent with environments where larger, weakly coated BC cores contribute preferentially to absorption. M_c exerts negligible influence in Dhaka but is associated with cooling negative SHAP contribution in Xuzhou only at high loading (>450 mg m^{-2}), consistent with enhanced scattering associated with heavily polluted industrial environments. Overall, while $BCAOD_{550}$ remains the most influential predictor, mixing state emerges as a strong modulator of predictor BC TOA transition regimes under intermediate forcing conditions, with N_c exerting a strong impact under high BC TOA regimes in the learned mapping.

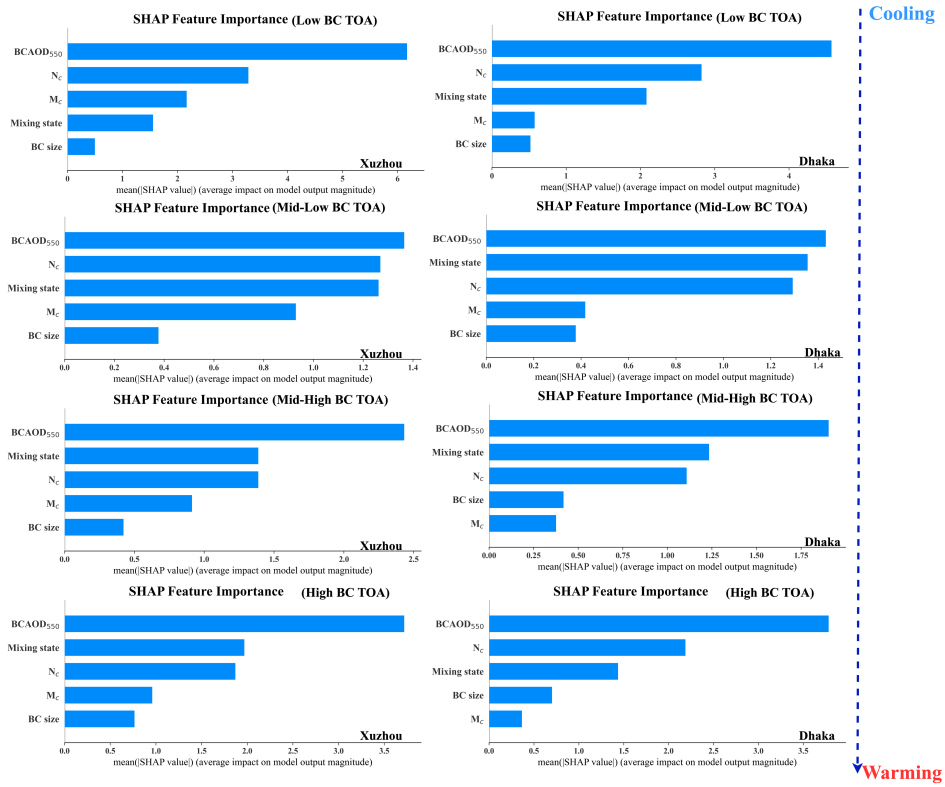

Figure S6: Shapley Additive Explanations (SHAP) analysis showing the feature importance and feature ranking through mean SHAP values for predicting TOA over Xuzhou and Dhaka for different transitional ranges of BC TOA forcing

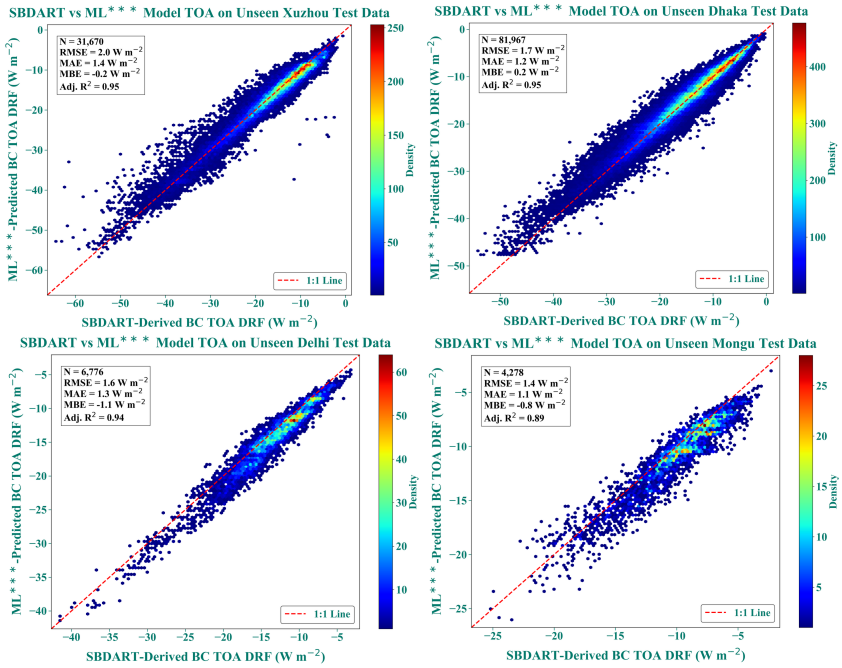

Figure S7: Performance of the revised combined model (ML***) on held-out test data across the four regions (30% from each region, 124,691 total samples, completely unseen during training). Panels show SBDART-derived vs ML***predicted BC TOA DRF

Figure S8: Photographs of Xuzhou under high aerosol loading, taken within minutes of each other using identical camera settings (12 mm, f/1.8, ISO 50), with only a slight shutter-speed adjustment to avoid sensor saturation when facing the Sun. Panel (a) shows the view toward the Sun (not directly at it), where strong forward scattering produces dense haze and reduced visibility (2024-10-15 07:42 local time). Panel (b) shows the view in the opposite direction, where apparent scattering and haze are noticeably weaker and visibility is enhanced (2024-10-15 07:44 local time). The pronounced directional contrast qualitatively illustrates anisotropic scattering under heavy aerosol loading, providing visual context for the microphysics-driven absorption–scattering competition discussed in the main text. Photo courtesy: Prof. Jason Blake Cohen.

References:

Dubovik, O. and King, M. D.: A flexible inversion algorithm for retrieval of aerosol optical properties from Sun and sky radiance measurements, Journal of Geophysical Research: Atmospheres, 105, 20673–20696, https://doi.org/10.1029/2000JD900282, 2000.

Dubovik, O., Smirnov, A., Holben, B. N., King, M. D., Kaufman, Y. J., Eck, T. F., and Slutsker, I.: Accuracy assessments of aerosol optical properties retrieved from Aerosol Robotic Network (AERONET) Sun and sky radiance measurements, Journal of Geophysical Research: Atmospheres, 105, 9791–9806, https://doi.org/10.1029/2000JD900040, 2000.

Dubovik, O., Sinyuk, A., Lapyonok, T., Holben, B. N., Mishchenko, M., Yang, P., Eck, T. F., Volten, H., Muñoz, O., Veihelmann, B., van der Zande, W. J., Leon, J.-F., Sorokin, M., and Slutsker, I.: Application of spheroid models to account for aerosol particle nonsphericity in remote sensing of desert dust, J. Geophys. Res., 111, D11208, https://doi.org/10.1029/2005JD006619, 2006.

Fu, Y., Zhu, J., Yang, Y., Yuan, R., Liu, G., Xian, T., and Liu, P.: Grid-cell aerosol direct shortwave radiative forcing calculated using the SBDART model with MODIS and AERONET observations: An application in winter and summer in eastern China, Adv. Atmos. Sci., 34, 952–964, https://doi.org/10.1007/s00376-017-6226-z, 2017.

Liu, Y., Yan, C., and Zheng, M.: Source apportionment of black carbon during winter in Beijing, Science of The Total Environment, 618, 531–541, https://doi.org/10.1016/j.scitotenv.2017.11.053, 2018.

Luo, J., Li, Z., Qiu, J., Zhang, Y., Fan, C., Li, L., Wu, H., Zhou, P., Li, K., and Zhang, Q.: The Simulated Source Apportionment of Light Absorbing Aerosols: Effects of Microphysical Properties of Partially-

Coated Black Carbon, Journal of Geophysical Research: Atmospheres, 128, https://doi.org/10.1029/2022JD037291, 2023.

Patel, P. N., Dumka, U. C., Babu, K. N., and Mathur, A. K.: Aerosol characterization and radiative properties over Kavaratti, a remote island in southern Arabian Sea from the period of observations, Science of The Total Environment, 599–600, 165–180, https://doi.org/10.1016/j.scitotenv.2017.04.168, 2017.

Paulescu, M., Paulescu, E., Gravila, P., and Badescu, V.: Solar Radiation Measurements, 17–42, https://doi.org/10.1007/978-1-4471-4649-0_2, 2013.

Ricchiazzi, P., Yang, S., Gautier, C., and Sowle, D.: SBDART: A Research and Teaching Software Tool for Plane-Parallel Radiative Transfer in the Earth's Atmosphere, Bull. Am. Meteorol. Soc., 79, 2101–2114, https://doi.org/10.1175/1520-0477(1998)079<2101:SARATS>2.0.CO;2, 1998.